Combustion, Explosion, and Shock Waves, Vol. 45, No. 5, pp. 518–529, 2009

Flowfield-Flame Structure Interactions in an Oscillating Swirl Flame

R. Sadanandan,[1] M. Stöhr,[1] and W. Meier[1]

UDC 536.46

Translated from *Fizika Goreniya i Vzryva*, Vol. 45, No. 5, pp. 16–28, September–October, 2009.
Original article submitted October 25, 2008.

A swirling methane–air diffusion flame at atmospheric pressure is stabilized in a gas turbine model combustor with good optical access. The investigated flame with a thermal power of 10 kW and an overall equivalence ratio of 0.75 exhibits pronounced thermoacoustic oscillations at a frequency of 295 Hz. The main goal of the presented work is a detailed experimental characterization of the flame behavior in order to better understand the flame stabilization mechanism and the feedback loop of thermoacoustic instability. OH* chemiluminescence imaging is applied for determining the flame shape and estimating the heat release rate. Laser Raman scattering is used for simultaneous detection of the major species concentrations, mixture fractions, and temperature. The velocity fields are measured by particle image velocimetry (PIV) or stereo PIV, simultaneously with OH planar laser-induced fluorescence. The dynamic pressure in the combustion chamber is determined by microphone probes. The flowfield exhibits a conically shaped inflow of fresh gases and inner and outer recirculation zones. The instantaneous flame structures are dominated by turbulent fluctuations; however, phase-correlated measurements reveal phase-dependent changes in all measured quantities. The paper presents examples of measured results, characterizes the main features of the flame behavior, explains the feedback loop of the oscillation, and discusses the flame stabilization mechanism.

Key words: oscillating swirl flame, laser-induced fluorescence, flame stabilization, Raman scattering.

INTRODUCTION

Swirl flames are used extensively in practical combustion systems because they enable a high degree of energy conversion in a small volume and exhibit a good ignition and stabilization behavior over a wide operating range [1–3]. They are mostly used as premixed or partially premixed flames in stationary gas turbine combustors and as diffusion flames in aero engines. To reduce NO$_x$ emissions, the flames are operated generally very lean [4–7]. Under these conditions, the flames tend to exhibit undesired instabilities, e.g., in the form of unsteady flame stabilization or thermoacoustic oscillations [8–13]. The underlying mechanisms of the instabilities are based on the complex interaction between flowfield, pressure, mixing, and chemical reactions, and are not very well understood to date. Under these conditions, combustion is governed by a complicated turbulent flowfield and strong effects of turbulence-chemistry interactions. One question of interest is the flame stabilization mechanism. It is known that the mixing of recirculating exhaust gases with the fresh gas plays an important role for flame stabilization; however, the details of this process are not clear. Another important question concerns the nature of the feedback mechanism of periodic combustion instabilities. The basic ideas of different feedback mechanisms have been reviewed by Lieuwen and Yang [14], but in most cases the details of the chain of events are not understood.

The investigations presented in this paper were performed at atmospheric pressure in a gas turbine model combustor with an optical combustion chamber, which

---

[1] Institut für Verbrennungstechnik, Stuttgart, 70569; Rajesh.Sadanandan@dlr.de.

0010-5082/09/4505-0518

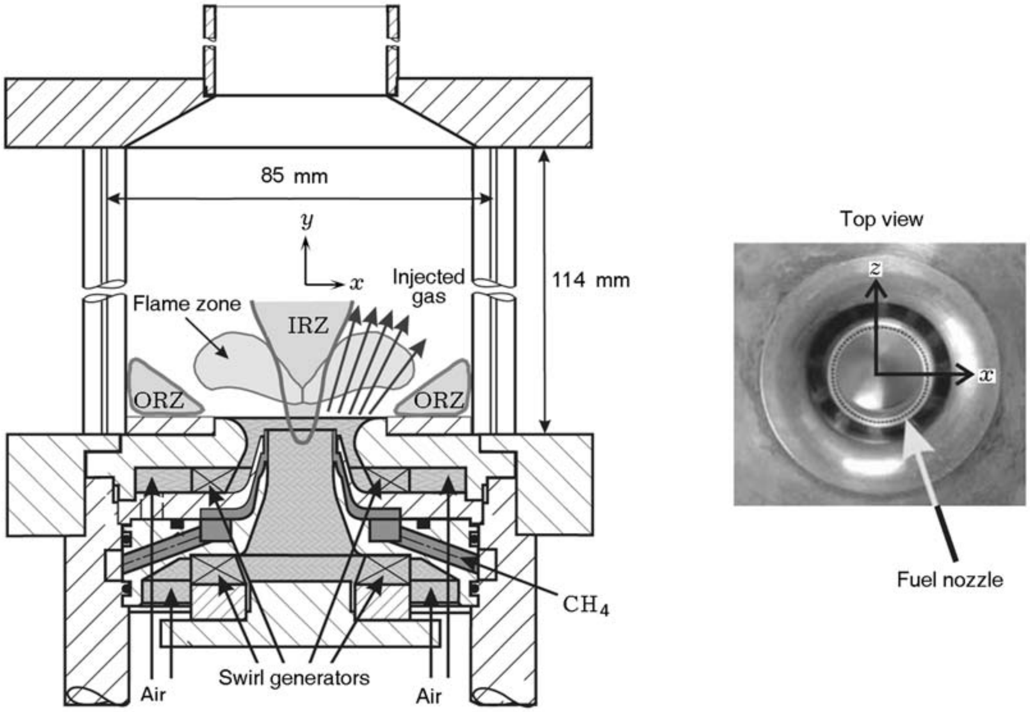

Fig. 1. Schematic drawing of the gas turbine model combustor: IRZ and ORZ are the inner and outer recirculation zones, respectively.

has been used in different studies before [15–23]. Under certain operating conditions, the flame exhibits strong periodic thermoacoustic pulsations at a frequency of ≈295 Hz. To investigate the mechanisms leading to flame stabilization and pulsations, various non-intrusive optical and laser measuring techniques were applied in combination with dynamic pressure measurements. Particle image velocimetry (PIV) and stereoscopic PIV were applied for 2D and 3D measurements of the flowfield, respectively. The flame structures were measured by planar laser-induced fluorescence of OH (OH-PLIF) and by chemiluminescence imaging. Further information about the thermochemical state of the flame was gained by using the laser Raman scattering.

1. GAS TURBINE MODEL COMBUSTOR AND DIAGNOSTIC SETUP

The measurements were performed in an optically accessible gas turbine model combustor, which is a modified gas turbine combustor originally equipped with an air blast nozzle for liquid fuels [24]. In the current measurements, a non-premixed methane–air flame is stabilized under fuel-lean conditions. The combustor is schematically illustrated in Fig. 1. Co-swirling dry air fed from a common plenum at room temperature and pressure was supplied to the flame through a central nozzle (diameter 15 mm) and an annular nozzle (inner diameter 17 mm and outer diameter 25 mm) contoured to an outer diameter of 40 mm (see the top view in Fig. 1). The plenum chamber had an inner diameter of 79 mm and a height of 65 mm. The radial swirlers in the central and annular nozzles consisted of 8 and 12 channels, respectively, resulting in an air mass flow ratio of approximately 1.5 between the annular and central nozzles. Non-swirling CH$_4$ was fed into the combustion chamber through 72 channels (0.5×0.5 mm), forming a ring between the air nozzles. The reference height ($y = 0$) was defined at the exit plane of the outer air nozzle, which was at a height of 4.5 mm above the exit planes of the fuel and central air nozzles. A contoured steel top plate with a central exhaust tube (diameter 40 mm and length 50 mm) formed the exhaust gas exit. The combustion chamber had a square section of 85×85 mm and a height of 114 mm. It was equipped with four quartz windows held by four rods (diameter 10 mm) in the corners, thereby enabling excellent optical access to the flame zone. Air ventilators were used on the four sides of the combustion chamber to avoid excessive overheating of the quartz windows. The high velocity in the exhaust tube prevented any backflow from outside the combustion chamber.

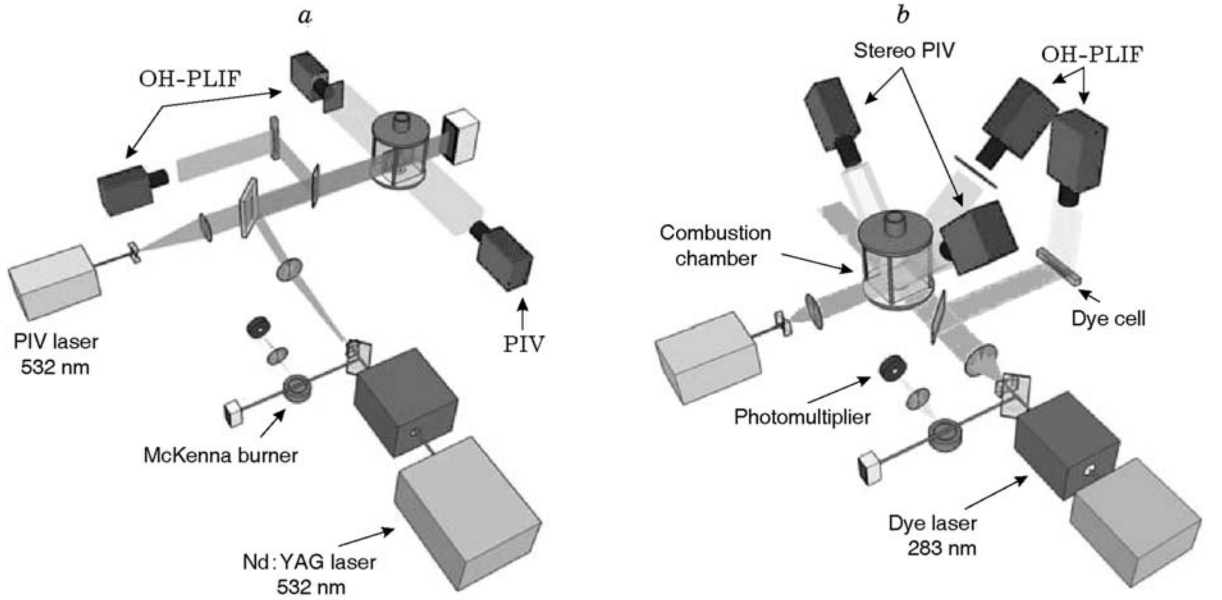

Fig. 2. Schematic drawing of the optical setup used for simultaneous OH-PLIF and PIV measurements in the vertical (a) and horizontal (b) orientation.

The flame investigated had a thermal power of 10.3 kW and an overall equivalence ratio $\phi = 0.75$. The corresponding CH_4 and air mass flow rates, regulated by a high-precision Coriolis controller (Siemens Mass 2100) and a mass flow controller (Bronkhorst), were 12.3 and 281 g/min, respectively. The flame exhibited pronounced thermoacoustic oscillations at a frequency of $\approx$295 Hz. Microphones (Bruel and Kjaer 4939) mounted in the plenum chamber and to the combustion chamber, at a height of 16 mm in one of the four rods that held the quartz windows, were used for recording the acoustic pressure oscillations. The nozzle Reynolds number based on the cold inflow and the minimum outer nozzle diameter (25 mm) was about 15,000, and the swirl number of the burner calculated from the velocity profile just above the burner was 0.55 [21].

For pointwise quantitative measurements of the major species concentrations (O_2, N_2, CH_4, H_2, CO, CO_2, and H_2O) and temperature, laser Raman scattering was applied. The radiation of a flashlamp-pumped dye laser (Candela LFDL 20, wavelength $\lambda = 489$ nm, pulse energy $E_p \approx 0.3$ J, and pulse duration $\tau_p \approx 3\ \mu$sec) was focused into the combustion chamber, and the Raman scattering emitted from the measuring volume (length 0.6 mm and diameter 0.6 mm) was collected by an achromatic lens ($D = 80$ mm and $f = 160$ mm) and relayed to the entrance slit of a spectrograph (SPEX 1802, $f = 1$ m, slit width 2 mm, and dispersion 0.5 nm/mm).

The dispersed and spatially separated signals from different species were detected by individual photomultiplier tubes in the focal plane of the spectrograph and sampled by boxcar integrators. The species number densities were calculated from these signals, based on calibration measurements, and the temperature was deduced from the total number density via the ideal gas law. Simultaneous detection of all major species with each laser pulse also allowed the instantaneous mixture fractions to be determined. Details of the measuring system are described elsewhere [13, 21].

A schematic drawing of the experimental setup used for simultaneous PIV and OH-PLIF measurements is shown in Fig. 2. Two different orientations of the light sheet were employed during the measurements: in the vertical plane along the flame axis where 2D PIV measurements were performed and in the horizontal plane orthogonal to the flame axis at three axial locations $y = 5$, 10, and 20 mm where 3D (stereoscopic) PIV measurements were performed. The present paper describes only the results for $y = 5$ mm.

The laser system used for OH-PLIF measurements consisted of a frequency doubled Nd:YAG laser (Spectra Physics, Quanta Ray PIV system) pumping a tunable dye laser (Sirah Precisionscan G-24) at 10 Hz. The frequency doubled output of the dye laser was tuned to the $Q_1(8)$ transition of OH at $\lambda = 283$ nm in the $\nu'' = 0$, $\nu' = 1$ vibrational band of the $A^2\Sigma^+ - X_2\Pi$ system. The population of the laser-coupled ground state of the selected line varied by approximately 9% in the temperature range of interest (1400–2200 K). The UV beam with a pulse energy of approximately 2–2.5 mJ at the laser exit was expanded into a sheet of ≈60 mm in height and 400 μm thickness at the burner axis, using a combination of cylindrical and spherical lenses.

The OH fluorescence in the $\nu' = 1$, $\nu'' = 1$ and $\nu' = 0$, $\nu'' = 0$ bands near $\lambda = 310$ nm was detected by means of an interference filter in the wavelength region $\lambda = 295$–340 nm, which also aided in blocking the unwanted scattered laser lights from OH-PLIF and PIV lasers and background radiations. Online monitoring of the excitation line was achieved by diverting a small portion of the incoming UV beam into a methane–air reference flame stabilized on a McKenna burner, operated under laminar conditions, and observing the intensity of the OH-PLIF produced using a photomultiplier. The shot-to-shot variations in laser sheet profiles were corrected by sending a part of the incoming laser beam onto a dye cell filled with a fluorescent dye. The fluorescence emitted by this dye solution was imaged simultaneously with the OH-PLIF images and was used for correcting the laser sheet inhomogeneities in the image post-processing procedure.

The OH-PLIF detection system consisted of two image intensified CCD cameras (LaVision Image Intense, 1376×1040 pixels), one for the OH-PLIF imaging and the other for the sheet profile imaging. The OH-PLIF camera was equipped with an achromatic UV lens (Halle, $f/2$, $f = 64$ mm) and the sheet profile camera had a Nikon objective ($f/4$, $f = 50$ mm). OH* chemiluminescence was also imaged with the same detection system along with the filter combination. The exposure time for the OH-PLIF imaging was 400 nsec, whereas for OH* chemiluminescence it was 40 μsec.

In case of PIV measurements, the laser system used was a frequency doubled Nd : YAG laser (New Wave Solo PIV 120) with a pulse energy of 120 mJ at $\lambda = 532$ nm. The pulse delay between the two laser shots was 16 μsec, and the flow was seeded with TiO_2 particles with a nominal diameter of 1 μm. The laser beam was expanded into a sheet of 60 mm in height and 1 mm in thickness inside the combustor using a combination of cylindrical lenses. The spatial resolution of the velocities was 0.77 mm (corresponding to an interrogation region of 12×12 pixels) in both direction. The detection system consisted of two double-shutter CCD cameras (LaVision Image Intense, 1376×1024 pixels), both equipped with Nikon objectives ($f/5.6$, $f = 50$ mm). The vector fields were generated using the commercially available PIV software from LaVision (Flow Master).

The time synchronization between different laser sources and detection systems was achieved using a programmable timing unit (PTU) from LaVision and two pulse delay generators (BNC, Model 555). The framing rate for both OH-PLIF and PIV imaging was 5 Hz. The OH-PLIF image was captured 10 μsec after the first PIV laser pulse. This time delay also helped in mitigating the laser light scattering effects from the PIV camera, in addition to providing simultaneous OH-PLIF images with the velocity fields. The microphone signals from the plenum and combustion chambers were fed into a multichannel analog-to-digital converter along with the Q-switch trigger from the lasers during the measurements for identifying the phase angle φ of each acquired OH-PLIF and PIV image. The phase angle definition here is such that the pressure minimum in the plenum chamber is taken as $\varphi = 0$, and the negative-to-positive transition is taken as $\varphi = 90°$, etc.

2. RESULTS AND DISCUSSION

2.1. Ensemble-Averaged Flame and Flowfield Characteristics

The ensemble-averaged velocity vectors overlapped over the corresponding streamlines of the flowfield in the axial plane ($z = 0$) and in the horizontal plane ($y = 5$ mm) are shown in Fig. 3a. The axial plot shows a flowfield typical of enclosed swirl burners, namely, an inner recirculation zone (IRZ), an outer recirculation zone (ORZ), and a conically shaped inflow of fresh gases. There are two shear layers formed, one between the fresh gases and IRZ, and the second one between ORZ and the fresh gases. The instantaneous plots, however, highlighted a different picture. It was seen that small-scale vortical structures were formed at the inner and outer shear layers, and these vortical structures promoted intense mixing between the fresh gases and the burned gases, thereby playing a vital role in flame stabilization and ignition of fresh mixtures [23]. The axial velocity vectors v_y overlapped over the streamlines in the horizontal plane show an axisymmetric flowfield at $y = 5$ mm. There is a strong inflow of fresh gases visible in the radial region $x \approx 6$–20 mm and a recirculating downward flow in IRZ up to a radius of $x \approx 6$ mm.

Figure 3b shows the ensemble-averaged OH* (electronically excited) chemiluminescence and OH-PLIF images, averaged from 500 single-shot images in the vertical orientation. The OH* emissions integrated along the line of sight provide information about the shape and spatial position of the heat release zone, as the near UV spontaneous emissions from OH* is visible only in the heat release zone.

Also, the flame is seen to stabilize at a height of $y \approx 2$ mm, pointing to a partially premixed flame with a significant level of mixing on the way from the fuel

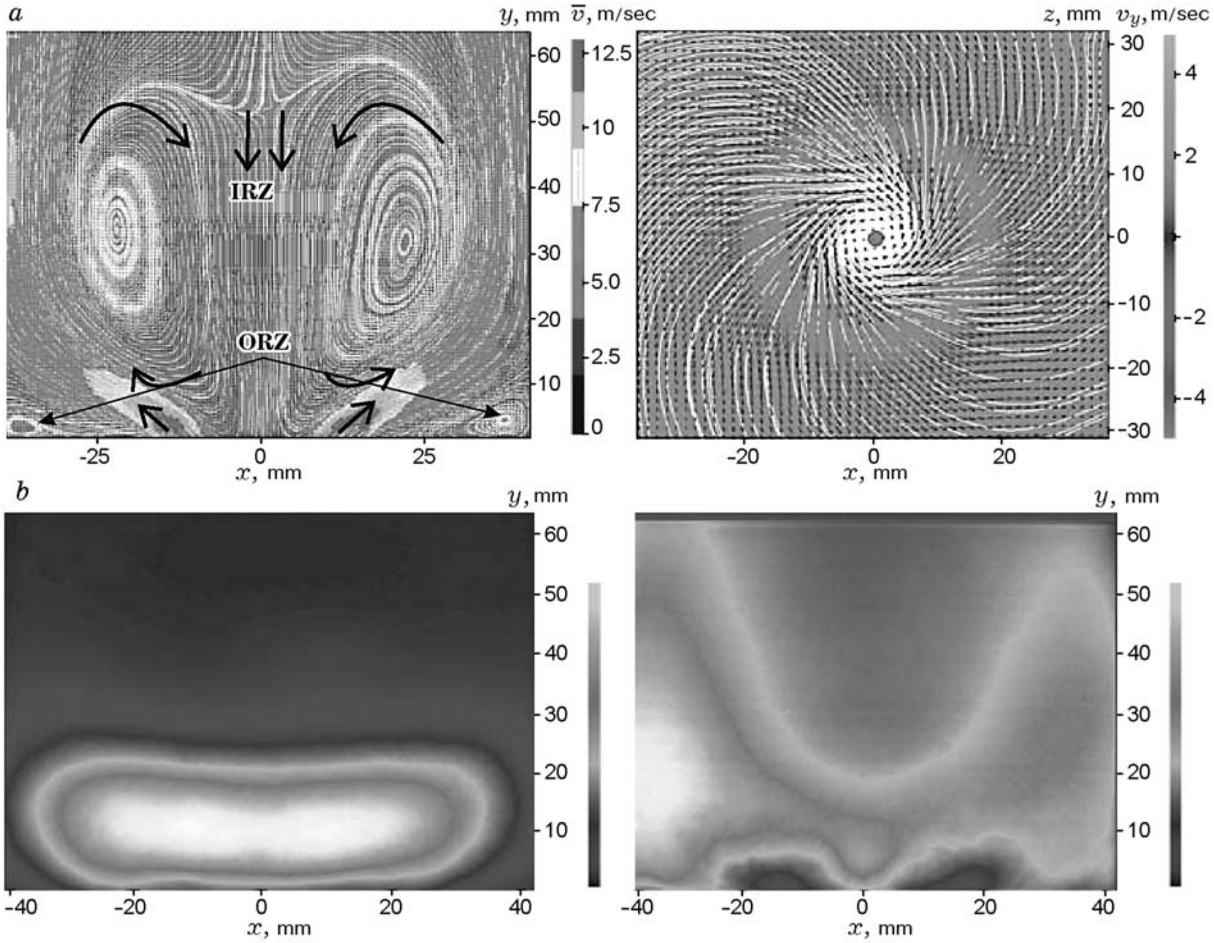

Fig. 3. Ensemble-averaged velocities ($\bar{v}$) overlapped over the streamlines in the axial plane (a, left) and axial velocities v_y overlapped over the streamlines in the horizontal plane $y = 5$ mm (a, right). Ensemble-averaged OH* chemiluminescence (b, left) and OH-PLIF image (b, right) in the vertical orientation.

nozzle ($y = -4.5$ mm) to the flame. The flame is rather flat with the region of the maximum heat release extending from 5 to 20 mm in the vertical direction. The disparity in the intensities seen between the left and right parts of the OH-PLIF image in Fig. 3b was due to absorption by OH radicals, which was ≈44% in our measurements. The absorption was determined by taking the average fluorescence intensities in two rectangular regions (5 mm wide and 10 mm high), 5 mm from the left and right sides of the quartz windows at a height $y = 30$ mm. To reduce the influence of absorption and fluorescence trapping errors in the interpretation of experimental results, only the left parts of the vertical OH-PLIF images and the bottom left quarters of the horizontal OH-PLIF images are used in the following sections.

The OH radicals can be used as a marker for high-temperature regions like reaction zones or regions of burned gases where the temperatures are $\geqslant$1400 K. Thus, the dark region seen in the vertical OH-PLIF image represents the cold fuel–air mixture. Through comparisons with the OH* images, it can be concluded that the LIF intensities seen above $y = 25$ mm are caused by the presence of hot burned gases rather than by the presence of reaction zones.

Figure 4 shows the instantaneous images with the PIV plot overlapped over the OH-PLIF image in the vertical orientation along the axial plane ($z = 0$) and in horizontal orientation at $y = 5$ mm. No strong intensity gradients are visible at IRZ above $y = 25$ mm, indicating the absence of reaction zones. From previous temperature measurements, it is known that the temperature in this region is around 1950 K with negligible rms fluctuations, testifying to a region of burned gases. As the LIF intensities registered here are relatively low in comparison to the shear layer regions, the

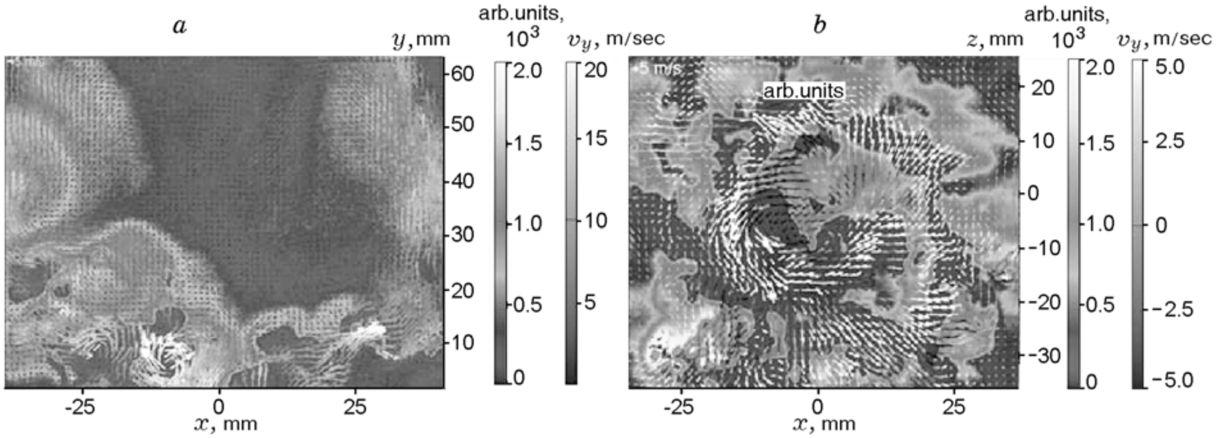

Fig. 4. Instantaneous OH-PLIF and PIV images in the axial plane at $z = 0$ (a) and in the horizontal plane at $y = 5$ mm (b).

OH concentrations in IRZ should be in chemical equilibrium. From the OH-PLIF image, one can get a good impression of the turbulence level present at the burner exit. The wrinkled flame structures in the vertical OH-PLIF image are more or less continuous in the 2D plane, like the flames in the laminar regime. The flame structures in the horizontal plane near to the inner and outer shear layers, however, are highly wrinkled and contain isolated regions of ignition and extinction, highlighting the strong interplay between turbulence and chemical reactions, leading to finite-rate chemistry effects in this region.

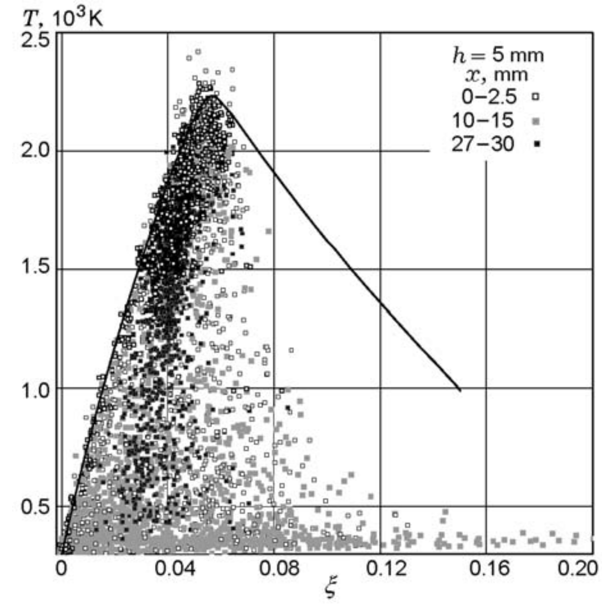

Fig. 5. ξ–T Correlations obtained from Raman scattering measurements at $y = 5$ mm (the curve shows the adiabatically equilibrium temperature).

2.2. Turbulence-Chemistry Interactions

More information on the thermochemical state of the system can be obtained from Raman scattering measurements. Figure 5 shows the temperature (T) and mixture fraction (ξ) correlation obtained from Raman scattering measurements at $y = 5$ mm on the same burner with similar operating conditions of fuel and air mass flow rates [18, 22, 25]. Each symbol represents the result of a single-shot measurement, and the solid curve is obtained by adiabatic flame calculations. It can be seen that the investigated flame exhibits a wide range of ξ–T combinations under such operating conditions. A large number of samples in the scatter plot lie between $\xi = 0$–0.1, highlighting the fast mixing achieved in such short distances. In IRZ ($x = 0$–5 mm) and ORZ ($x = 27$–30 mm), most of the samples lie close to the calculated curve, indicating a completely reacted mixture. In the inflow region ($x = 10$–15 mm), however, one can see samples covering a wide range of $\xi - T$ combinations with ξ both above and below the global ξ value of 0.0418 and intermediate temperatures. The wide range of T comes from mixing of the cold fuel–air mixture with the hot burned gases in the inner and outer shear layer regions. There could be two possibilities for the existence of samples with intermediate temperatures. The first one could be from mixing of the fresh gas with the hot gases, which rises the mixture temperature to intermediate levels. The second reason could be due to local flame extinctions, which results in mixtures with temperatures far below the adiabatic temperature.

2.3. Acoustic Measurements

The investigated flame exhibited strong thermoacoustic oscillations at a frequency $f = 295$ Hz. Figure 6 shows the pressure oscillations in the plenum and combustion chambers at different values of the phase φ of the acoustic oscillations. It is interesting to note that the maximum acoustic pressure in the plenum chamber ($p_a = 292$ Pa at $\varphi = 180°$) is greater than the acoustic pressure in the combustion chamber ($p_a = 125$ Pa at $\varphi = 135°$). The pressure oscillations in the plenum chamber are phase-shifted by about 45°, as compared to the pressure oscillations in the combustion chamber. The figure also shows the corresponding phase-averaged global heat release, calculated by taking the average chemiluminescence intensity in a rectangular region covering the heat release zone in OH* chemiluminescence images at different φ. The value of φ corresponding to the maximum heat release matches the maximum pressure oscillations in the combustion chamber, in accordance with the Rayleigh criterion for self-sustained oscillations. The acoustic pressure difference between the plenum and the combustion chambers (δp) at different phase angles φ are also plotted in Fig. 6. The value of δp, which reaches a maximum at $\varphi \approx 225°$, is seen to have a strong effect on acceleration of the fresh fuel–air mixture into the combustion chamber and thereby on the feedback mechanism of the combustion instability itself, as it will be seen in the following sections.

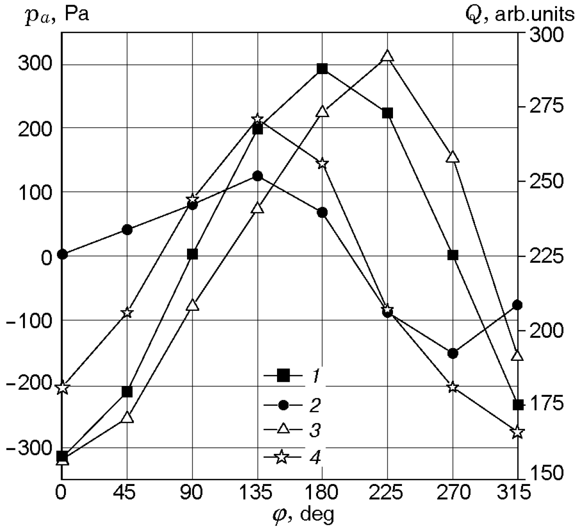

Fig. 6. Relationship between the variations of acoustic pressure oscillations in the plenum and combustion chambers with the global heat release at different phase angles of acoustic pressure oscillations: 1) plenum chamber; 2) combustion chamber; 3) pressure difference δp; 4) heat release.

2.4. Phase-Resolved Velocity and Temperature Profiles

The flame shape, heat release, velocity, and temperature distributions varied significantly during an oscillation cycle of the acoustic pressure. However, the instantaneous images were dominated by stochastic turbulent fluctuations. To reveal phase-dependent changes, single shot results belonging to the same phase angle were averaged. The distributions of the average velocity (at $y = 5$ mm and phase angles $\varphi = 135$ and 315°) and its axial component v_y (in the contour plot) overlapped over the OH-PLIF image, are shown in Fig. 7. It is clear from the figures that the highest OH concentrations appear at regions near the inner and outer shear layers where the inflow velocities are moderate. These regions probably correspond to the flame zone. The inflow velocities vary significantly with φ, and IRZ is shrunk to a very intense region of burned gases with high temperatures (see discussions above) as φ changes from 135 to 315°. Figure 8 shows the axial and radial velocity profiles deduced from the vertical PIV vector plots at a height $y = 2$ mm for eight phase angles. In these plots, strong periodic variations of the flowfield with φ are clearly visible. These plots can also be used to infer qualitative information about the volumetric discharge at $y = 2$ mm. Based on variations in velocity at different φ, one can predict that there will also be a strong variation in the volumetric discharge of the fresh fuel–air mixture during one complete acoustic cycle. The variations are more profound in the inflow region, with the minimum discharge at $\varphi = 135°$ and the maximum discharge at $\varphi = 315°$. Similar trends can also be seen in IRZ where there is a strong reverse flow at $\varphi = 135°$ and a minimum reverse flow at $\varphi = 315°$. From a comparison with δp plotted in Fig. 6, it can be noted that the periodic variations of the flowfield and the mass transport are affected by the pressure oscillations in the plenum and combustion chambers. This trend is visible in the axial and radial velocity profiles. In the inflow region $x \approx 7$–18 mm), the maximum axial and radial velocities are recorded between $\varphi = 270°$ and 0, which means that the maximum axial velocity at $\varphi = 315°$ follows approximately 90° after the maximum δp at $\varphi = 225°$. This behavior is plausible if one considers a sinusoidal form for the acoustic velocity. Then the velocity variations due to acceleration are phase-shifted by 90°, which fits well the maximum velocities. This also confirms the influence of periodic oscillations, which, in turn, are driven

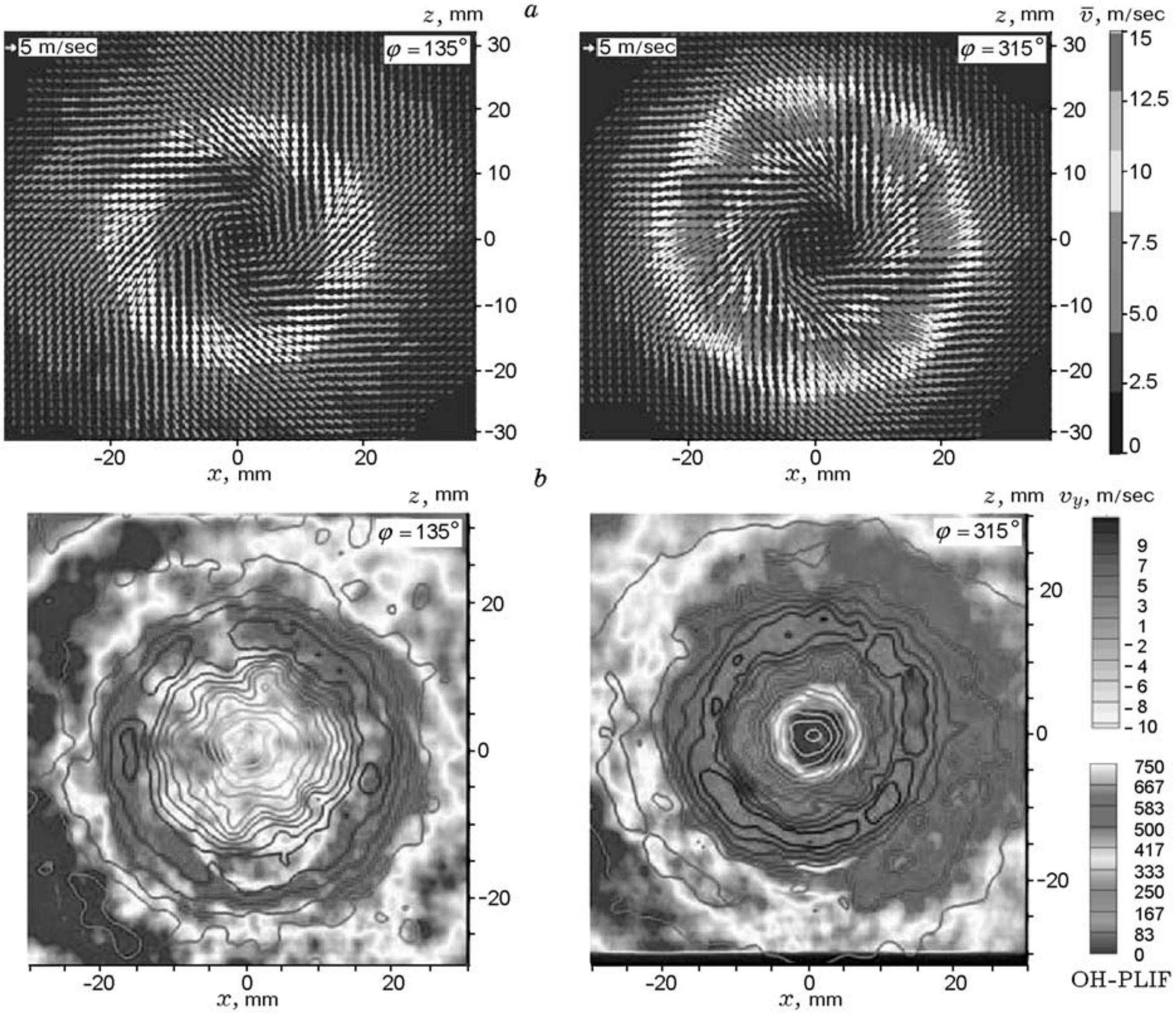

Fig. 7. Distributions of the average velocity $\bar{v}$ (a) and its axial component v_y overlapped over the corresponding OH-PLIF distributions for two phase angles of acoustic pressure oscillations at $y = 5$ mm (b).

by the periodic heat release in the combustion chamber, on the mass transport. The strongest variations in the axial velocity are seen in IRZ (0–6 m/sec at $x = 0$) and in the inflow region (6–14 m/sec at $x = 7$–18 mm), whereas the variations in the radial velocities are strong in ORZ and in the beginning of the inflow region (0–3 and 6–13 m/sec, respectively). At $\varphi = 270$ and 315°, the axial and radial positive velocities reach their maximum values in the inflow region, whereas the maximum negative velocity is observed in IRZ ($x = 0$) at $\varphi = 135$ and 180° and in ORZ ($x = 20$–30 mm) at $\varphi = 45°$. That is, the highest inflow velocities happen 90° after the maximum of δp.

The radial profiles of the mean temperature T at $y = 5$ mm measured in Raman scattering experiments are shown in Fig. 9 [18, 25]. Strong variations in temperature are seen in IRZ ($T \approx 1000$ K) and in the inflow region ($x = 7$–18 mm, $T \approx 300$ K). The temperature in IRZ reaches a maximum at $\varphi = 270°$ and a minimum at $\varphi = 90$ and 135°. Interestingly, these values of φ also correspond to the minimum and maximum recirculation velocities at the axis, respectively (see Fig. 8). Similarly, at $\varphi = 135$ and 180°, the temperature reaches a maximum in the inflow region, which, in turn, coincides with the phase angle φ corresponding to the minimum axial velocity ($\varphi = 135°$). The temperature in the inflow region also reaches a minimum at $\varphi = 270$ and 315°, when the axial velocities are maximum. These variations in temperature with velocity at different values of φ reflect the influence of acoustic pressure oscillations, namely,

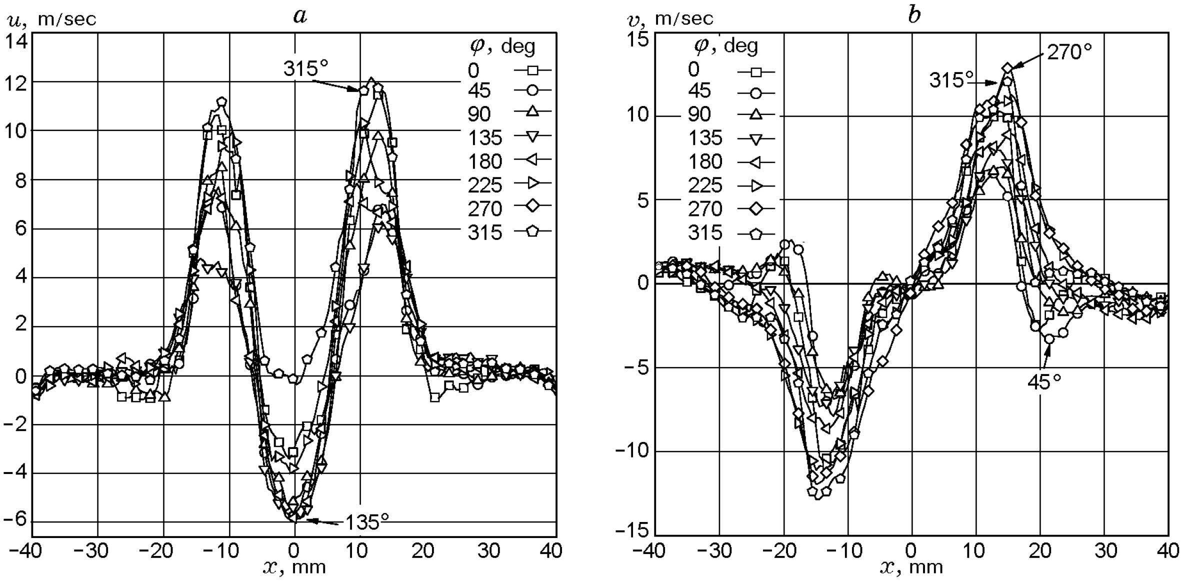

Fig. 8. Axial (a) and radial (b) velocity profiles deduced from PIV plots at $y = 2$ mm at different phase angles.

δp, on the thermochemical state of the system at each value of φ by influencing the mixing and reaction rate progress.

2.5. Phase-Resolved Heat Release Variations — Abel Deconvoluted OH* Chemiluminescence

Though OH* chemiluminescence images involve line-of-sight integration of intensity, ensemble-averaged OH* images can be reprocessed in the case of axisymmetric steady flames to obtain spatially resolved information. Figure 10 shows the Abel deconvoluted OH* chemiluminescence at $\varphi = 45, 135, 225$, and 315°, representing the mean OH* distribution in the vertical plane containing the flame axis. The heat release zone extends up to a height of ≈20–25 mm, with the region of the maximum heat release lying at $y = 10$–20 mm. At $\varphi = 135°$, with the maximum heat release, the flame zone extends almost to the walls of the combustion chamber, whereas it reaches only $x = 30$ mm at $\varphi = 315°$, with the minimum heat release. It should be noted (see Sec. 2.4) that the inflow velocity is at its minimum at $\varphi = 135°$ and at its maximum at $\varphi = 315°$. Thus, the heat release is half a period delayed, as compared to the inflow velocity (at $y = 2$ mm; Fig. 8). The maximum inflow velocity implies a maximum mass flow into the combustion chamber, because phase-dependent temperature variations are expected to be small in the inflow region at $y = 2$ mm. With an average convection velocity of ≈8 m/sec, the distance from the inflow region at $y = 2$ mm to the region of the main heat release at about $y = 15$ mm takes roughly 1.6 msec, which is close to half of the oscillation period $\tau/2 = 1.7$ msec. Thus, it is plausible that the heat release variations are induced by the varying mass flow in the inflow region, which, in turn, is triggered by the pressure difference between the

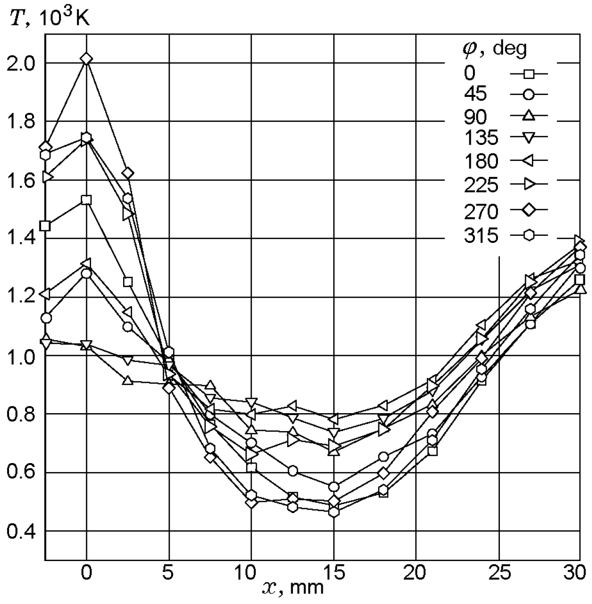

Fig. 9. Radial temperature profiles at $y = 5$ mm and different values of the phase of acoustic pressure oscillations [18].

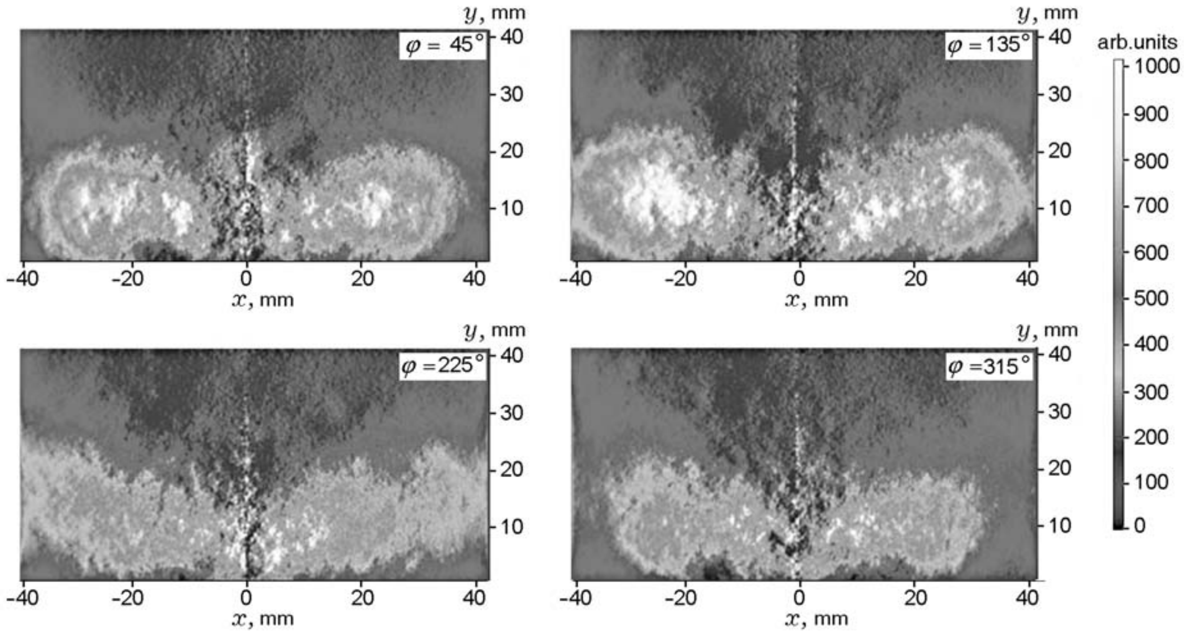

Fig. 10. Abel deconvoluted OH* chemiluminescence image at different values of the phase of acoustic pressure oscillations.

plenum and combustion chambers. This feedback loop is known as oscillating fuel supply combined with a convective time delay and has been observed for different combustors [13, 26, 27].

With respect to flame stabilization, the transport of hot combustion products within IRZ seems to play the dominant role. From Figs. 3 and 4 and also from the Raman scattering measurements, it is obvious that IRZ contains hot gases and that it reaches far down to or even into the central nozzle. The OH* distributions and single shot OH PLIF distributions [23] prove that combustion does occur in this region, in the shear layer between the inflow region and IRZ. Further downstream, combustion is not only restricted to this shear layer but is also seen in the region of the main inflow, as can be deduced from Figs. 3 and 10. At first glance, it seems surprising that the flame reactions can take place in the region of high inflow velocities. The results of this paper and experiments [23, 28] indicate that reacting fluid elements are convected from the shear layer into the inflow region. This process could be caused by vortex shedding or a precessing vortex core [23, 28]. Further, it is expected that a phase-dependent mixing rate of the hot gas from ORZ with the fuel–air mixture from the inflow region contributes to the reactivity of the mixtures and to flame stabilization [19]. Finally, phase-dependent changes in strain rates within the inflow region might also affect flame stabilization.

3. CONCLUSIONS AND OUTLOOK

A non-premixed CH_4–air flame has been operated in a gas turbine model combustor with good optical access. Various measuring techniques have been applied for the investigation, including chemiluminescence imaging, stereo PIV, laser Raman scattering, OH-PLIF, and dynamic pressure recording. At 10.3 kW thermal power and a global equivalence ratio of 0.75, the flame exhibits strong thermoacoustic oscillations at a frequency of $\approx$295 Hz. In this flame, the ensemble-averaged velocity fields and chemiluminescence images show a flowfield typical of enclosed swirl flames with inner and outer recirculation zones and a conical inflow region between them. The region of heat release is relatively short and extends only up to a height of 20–25 mm. Single shot PIV/PLIF measurements reveal that the instantaneous distributions of velocity and OH are dominated by turbulent structures with typical sizes of several millimeters. The thermochemical state of the flame, as deduced from Raman measurements, is characterized by considerable scatter in reaction progress reaching from non-reacted via partially reacted to completely reacted. The phase-correlated measurements show that all measured quantities vary with the acoustic frequency of the flame. The heat release, as deduced from the OH* distributions, is in phase with the pressure in the combustion chamber. The pressure in the plenum runs ahead of the pressure in the combustion chamber by about 45°, and the pressure difference is seen to trigger phase-dependent changes in the inflow velocity and, thus, the mass flow into the combustion chamber. The measured results lead to the conclusion that the varying inflow is the main reason for the varying heat release. In other words, the feedback loop of the oscillations is an oscillating fuel supply combined with a convective time delay.

With respect to the flame shape and stabilization mechanism, there remain open questions. It became obvious that the inner recirculation zone plays an important role by convecting hot combustion products to the flame root, as in many other swirl flames. One particular feature of this flame, however, is a rather flat shape and the occurrence of combustion reactions in the area of high inflow velocities. There are indications that reacting fluid elements are ripped from the inner shear layer and transported into the inflow region, thereby igniting and burning the fresh gases. The driving force for that process might be a precessing vortex core. Nevertheless, other effects, such as mixing of the hot gas from the outer recirculation zone into the injected fresh gas or phase-dependent changes of the turbulence scales, might also contribute to the flame shape. Combined PIV and OH-PLIF measurements with pulse repetition rates of several kilohertz are planned to yield a deeper insight into the complex processes.

The work has been financially supported within the DLR research project "Mehrskalen-Verbrennungssimulation."

REFERENCES

1. A. Gupta, D. Lilley, and N. Syred, *Swirl Flows*, Abacus Press, Kent (1984).
2. N. Syred and J. Beer, "Combustion in swirling flows: A review," *Combust. Flame*, **23**, 143–210 (1974).
3. R. Weber and J. Dugue, "Combustion accelerated swirling flows in high confinements," *Prog. Energ. Combust. Sci.*, **18**, 349–367 (1992).
4. S. Correa, "Power generation and aero propulsion gas turbines from combustion science to combustion technology," *Proc. Combust. Inst.*, **27**, 1793–1807 (1998).
5. A. Lefebvre, *Gas Turbine Combustion*, Taylor and Francis, Philadelphia (1999).
6. H. Bauer, "New low emission strategies and combustor designs for civil aero engine applications," *Prog. Comput. Fluid Dyn.*, **4**, 130–142 (2004).
7. K. Syed and E. Buchanan, "The nature of NO_x formation within an industrial gas turbine dry low emission combustor," in: *Proc. of ASME Turbo Expo*, GT-2005-68070, Nevada (2005).
8. J. Keller, "Thermoacoustic oscillations in combustion chambers of gas turbines," *AIAA J.*, **33**, 2280–2287 (1995).
9. C. Paschereit, K. Gutmark, and W. Weisenstein, "Structure and control of thermoacoustic instabilities in a gas turbine combustor," *Combust. Sci. Technol.*, **138**, 213–232 (1998).
10. S. Candel, "Combustion dynamics and control: Progress and challenges," *Proc. Combust. Inst*, **29**, 1–28 (2002).
11. J. Lee and D. Santavicca, "Experimental diagnostics for the study of combustion instabilities in lean premixed combustors," *J. Propuls. Power*, **19**, 735–750 (2003).
12. N. Syred, "A review of oscillation mechanisms and the role of precessing vortex core (PVC) in swirl combustion systems," *Prog. Energ. Combust. Sci.*, **32**, 93–161 (2006).
13. W. Meier, P. Weigand, X. Duan, and R. Giezendanner-Thoben, "Detailed characterization of the dynamics of thermoacoustic pulsations in a lean premixed swirl flame," *Combust. Flame*, **150**, 2–26 (2007).
14. T. Lieuwen and V. Yang (eds.), *Combustion Instabilities in Gas Turbine Engines: Operational Experience, Fundamental Mechanisms, and Modeling*, Amer. Inst. of Aeronautics and Astronautics, Inc., Reston, Virginia (2006).
15. R. Giezendanner, O. Keck, P. Weigand, W. Meier, U. Meier, W. Stricker, and M. Aigner, "Periodic combustion instabilities in a swirl burner studied by phase-locked planar laser-induced fluorescence," *Combust. Sci. Technol.*, **175**, 721–741 (2003).
16. X. Duan, P. Weigand, U. Meier, O. Keck, B. Lehmann, W. Stricker, and M. Aigner, "Experimental investigations and laser based validation measurements in a gas turbine model combustor," *Prog. Comput. Fluid Dyn.*, **4**, 175–182 (2004).
17. W. Meier, X. Duan, and P. Weigand, "Reaction zone structures and mixing characteristics of partially premixed swirling CH_4/air flames in a gas turbine model combustor," *Proc. Combust. Inst.*, **30**, 835–842 (2005).
18. X. R. Duan, W. Meier, P. Weigand, and B. Lehmann, "Phase-resolved laser Raman scattering and laser Doppler velocimetry applied to periodic instabilities in a gas turbine model combustor," *Appl. Phys. B*, **80**, 389–396 (2005).
19. P. Weigand, W. Meier, X. Duan, R. Giezendanner, and U. Meier, "Laser diagnostic study of the mechanism of a periodic combustion instability in a gas turbine model combustor," *Flow, Turbulence Combust.*, **75**, 275–292 (2005).
20. R. Giezendanner, U. Meier, W. Meier, J. Heinze, and M. Aigner, "Phase-locked two-line OH-PLIF thermometry in a pulsating gas turbine model combustor at atmospheric pressure," *Appl. Opt.*, **44**, 6565–6577 (2005).
21. P. Weigand, W. Meier, X. Duan, W. Stricker, and M. Aigner, "Investigations of swirl flames in a gas tur-

bine model combustor. I. Flow field, structures, temperature, and species distributions," *Combust. Flame*, **144**, 205–224 (2006).

22. W. Meier, X. Duan, and P. Weigand, "Investigations of swirl flames in a gas turbine model combustor II. Turbulence-chemistry interactions," *Combust. Flame*, **144**, 225–236 (2006).
23. R. Sadanandan, M. Stohr, and W. Meier, "Simultaneous OH-PLIF and PIV measurements in a gas turbine model combustor," *Appl. Phys. B*, **90**, 609–618 (2008).
24. M. Caom, H. Eickhoff, F. Joos, and B. Simon, "Influence of operating conditions on the atomisation and distribution of fuel by air blast atomizers," in: *ASME Propulsion and Energetics Panel 70th Symposium*, Crete 422 (1987), pp. 8.1–8.8.
25. P. Weigand, "Untersuchung periodischer Instabilitaten von eingeschlossenen turbulenten Drallflammen mit Lasermessverfahren," DLR Forschungsbericht 2007-19, Stuttgart (2007).
26. T. Sattelmayer, "Influence of the combustor aerodynamics on combustion instabilities from equivalence ratio fluctuations," *J. Eng. Gas Turbin. Power*, **125**, 11–19 (2003).
27. M. Zhu, A. Dowling, and K. Bray, "Forced oscillations in combustors with spray atomizers," *J. Eng. Gas Turbin. Power*, **124**, 20–30 (2002).
28. M. Stohr, R. Sadanandan, and W. Meier, "Experimental study of unsteady flame structures of an oscillating swirl flame in a gas turbine model combustor," *Proc. Combust. Inst.*, **32**, 2925–2932 (2009).